JCIM JOURNAL OF CHEMICAL INFORMATION AND MODELING

pubs.acs.org/jcim Article

Structure–Function Analysis of Resistance to Bamlanivimab by SARS-CoV-2 Variants Kappa, Delta, and Lambda

Shufeng Liu, Tien Huynh, Charles B. Stauft, Tony T. Wang,* and Binquan Luan*

Cite This: J. Chem. Inf. Model. 2021, 61, 5133–5140 Read Online

ACCESS | Metrics & More | Article Recommendations | Supporting Information

ABSTRACT: The newly emerging Kappa, Delta, and Lambda SARS-CoV-2 variants are worrisome, characterized with the double mutations E484Q/L452R, T478K/L452R, and F490S/L452Q, respectively, in their receptor binding domains (RBDs) of the spike proteins. As revealed in crystal structures, most of these residues (e.g., 452 and 484 in RBDs) are not in direct contact with interfacial residues in the angiotensin-converting enzyme 2 (ACE2). This suggests that albeit there are some possibly nonlocal effects, these mutations might not significantly affect RBD's binding with ACE2, which is an important step for viral entry into host cells. Thus, without knowing the molecular mechanism, these successful mutations (from the point of view of SARS-CoV-2) may be hypothesized to evade human antibodies. Using all-atom molecular dynamics (MD) simulation, here, we show that the E484Q/L452R mutations significantly reduce the binding affinity between the RBD of the Kappa variant and the antibody LY-CoV555 (also named as Bamlanivimab), which was efficacious for neutralizing the wild-type SARS-CoV-2. To verify simulation results, we further carried out experiments with both pseudovirions- and live virus-based neutralization assays and demonstrated that LY-CoV555 completely lost neutralizing activity against the L452R/E484Q mutant. Similarly, we show that mutations in the Delta and Lambda variants can also destabilize the RBD's binding with LY-CoV555. With the revealed molecular mechanism on how these variants evade LY-CoV555, we expect that more specific therapeutic antibodies can be accordingly designed and/or a precise mixing of antibodies can be achieved as a cocktail treatment for patients infected with these variants.

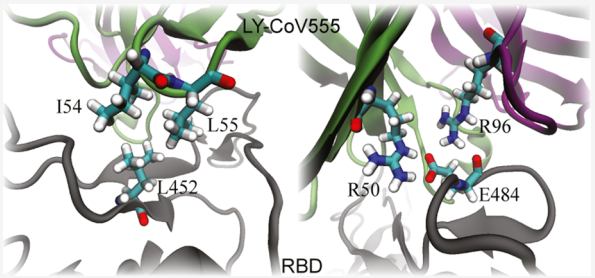

INTRODUCTION

The severe acute respiratory syndrome coronavirus 2 (SARS-CoV-2) that causes the ongoing COVID-19 pandemic has evolved into several new dominant variants with major genomic changes through mutations. Mutations in viruses arise (partly) as a result of low polymerase fidelity of viral replication but become a survival mechanism for viruses to adapt to new hosts and environments.[1] Although a majority of viral mutations are benign with most of them weeded out immediately, the current pandemic provides a suitable environment for SARS-CoV-2 to make natural selection of rare-acted but favorable mutations to strengthen its survival capability. Because the virus surface spike protein plays an important role in mediating SARS-CoV-2 entry into human cells and is the target for vaccine and therapeutic development, any mutations on this region may have biological significance, as it could affect the viral infectivity and antigenicity.[2−4] Indeed, experimental studies showed that the D614G mutation discovered at the earlier stage of the pandemic enhances the virus fitness and increases its transmission.[5,6] Similarly, the N501Y mutation found in the B.1.1.7 (Alpha), B.1.351 (Beta), and B.1.1.28.1 (Gamma) variants has been demonstrated to increase the binding affinity between the receptor-binding domain (RBD) and its human receptor ACE2 (hACE2), making these variants more transmissible.[7−9] Moreover, experimental and computational studies have showed that K417N and E484K found in the Beta variant could evade neutralization by many monoclonal antibodies (mAbs).[10,11]

Recently, a variant named B.1.617.1 (Kappa) that carries two mutations including L452R and E484Q has been designated as a variant of interest (VOI) by the World Health Organization (WHO), suggesting that this variant potentially could have higher transmissibility and severity or reinfection risk and is required continuous monitoring. In fact, the two mutations found in the Kappa variant are not completely new and have been seen in other variants separately. For example, the L452R mutation has been spotted in the B.1.427/B.1.429 variant, which is known to be more contagious and is capable of escaping antibody neutralization.[12] Also, the E484Q mutation is similar to E484K found in the Beta and Gamma variants. The latter were found to reduce neutralization by convalescent antisera and binding of some monoclonal

Received: August 31, 2021
Published: October 14, 2021

antibodies and increase the binding affinity to hACE2.[10,11] For the Kappa variant, this is the first time that these two mutations are found to coexist together, and therefore, it is important to understand how this variant could evade human antibodies or existing antibody drugs for treating COVID-19.

Complementary to ongoing experimental efforts, the all-atom molecular dynamics (MD) simulations with well-calibrated force fields have been widely used to explore the molecular mechanism of proteins.[13−16] In this work, we carried out both *in silico* modeling and *in vitro* experiment to investigate why a monoclonal antibody could neutralize the wild-type SARS-CoV-2 but failed to target the Kappa variant. Here, we focus on the drug LY-CoV555 that is a monoclonal antibody isolated from a convalescent COVID-19 patient. LY-CoV555 recognizes an epitope site in the RBD overlapping the binding site of hACE2 and was found to be efficacious on the wild-type SARS-CoV-2.[17] By combining all-atom MD, alchemical calculations, and experimental approach, we unveiled the molecular mechanism on how these two mutations in the Kappa variant can be evasive to LY-CoV555.

While we were finalizing this work, two additional variants named Delta (derived from the same lineage as Kappa) and Lambda had emerged and spread quickly worldwide. The Delta variant is characterized as the variant of concern due to the fact that it has become the dominant strain in many countries, while the Lambda variant has remained a VOI so far. Thus, we carried out similar studies for these two additional variants. We expect that these results provide invaluable insights for future designs of more efficacious mAbs to treat COVID-19 patients infected with the different variants and highlight the need for precision medicine (biologics) for each SARS-CoV-2 variant.

RESULTS

MD Simulations of the Complex of RBD and LY-CoV555. Figure 1a illustrates the simulation system for modeling the interaction between LY-CoV555 and the RBD (see the Methods section for detailed simulation protocols). According to our previous simulation of a different complex of the RBD and the Fab of the human antibody CB6,[9,18] the constant domains C^H in the heavy chain and C^L in the light chain (connected through disordered coils with their respective variable domains V^H and V^L) are not relevant for studying CB6's binding with the RBD. Thus, in this work, we only include the V^H and V^L domains of the Fab of LY-CoV555 in our simulation system, as shown in Figure 1a. This complex is very similar to the one in the crystal structure (PDB code: 7K43), showing that the RBD is bound with a Fab fragment (V^H and V^L only) of the antibody S2M11.[19] Our modeled complex (obtained from the crystal structure with a PDB code 7KMG) was solvated in a 0.15 M KCl electrolyte. Hereafter, we simply refer the variable domains that interact directly with the RBD as LY-CoV555. Additionally, we refer to the RBD of the variants as RBD-v.

During the 300 ns or so MD simulation, the complex of the RBD and LY-CoV555 starting from the structure in the crystal environment (PDB code: 7KMG) was properly equilibrated in the physiology-like environment (a 0.15 M electrolyte). Figure 1b shows the root-mean-square deviation (RMSD) of all protein backbone atoms in the complex. After about 50 ns, the RMSD values saturated at around 1.5 Å for the entire complex, suggesting that not only the secondary structure of each

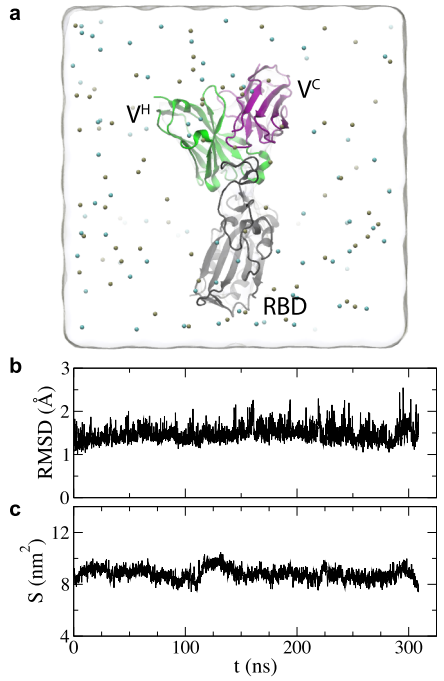

Figure 1. MD simulation systems. (a) Simulation setup for the complex of wild-type RBD and LY-CoV555 (a Fab fragment). Proteins are in the cartoon representation, with the RBD in gray and the V^H domain in the heavy chain of LY-CoV555 and the V^L domain in the light chain of LY-CoV555 in green and purple, respectively. K^+ and Cl^- are shown as tan and cyan balls, respectively. Water is shown transparently. (b) Time-dependent RMSD values for the complex (including only backbone atoms). (c) Time-dependent contact areas S between the RBD and V^H/V^L domains.

monomer (RBD, LY-CoV555's V^H or V^L) but also the whole trimer structure were very stable.

We further calculated the interfacial contact areas for the complex using the solvent accessible surface area (SASA) method.[20] By definition, the contact area is calculated by $(SASA_{LY\text{-}CoV555} + SASA_{RBD} - SASA_{complex})/2$. On average, Figure 1c shows that the contact area is about 8.8 nm^2. During the entire simulation time, values of contact areas fluctuated around the mean value, corroborating that the complex structure was stable. These results highlight that LY-CoV555 is an effective neutralizing antibody for the wild-type SARS-CoV-2.

To evaluate whether LY-CoV555 is still effective for the Kappa variant carrying the L452R and E484Q mutations, we further investigate the interfacial coordinations around L452 and E484. Remarkably, both L452 and E484 play an important role in stabilizing the interfacial binding, as shown in Figure 2. Figure 2a highlights the hydrophobic interactions between L452 in the RBD and I54/L55 in V^H of LY-CoV555, while Figure 2b signifies two interfacial salt bridges: (1) between E484 in the RBD and R50 in V^H of LY-CoV555; (2) between E484 in the RBD and R96 in V^L of LY-CoV555. These favorable interfacial interactions provide a molecular mechanism on how LY-CoV555 can be stably bound on the RBD.

From the analysis of simulation trajectory, we found that the electrostatic interaction energies are negligibly small (∼0 kcal/mol) and the total interaction energy between L452 and I54/L55 is dominated by the van der Waals (vdW) interactions, which is understandable because of the hydrophobic nature. Figure 2c shows that during the simulation, this interaction

https://doi.org/10.1021/acs.jcim.1c01058
J. Chem. Inf. Model. 2021, 61, 5133−5140

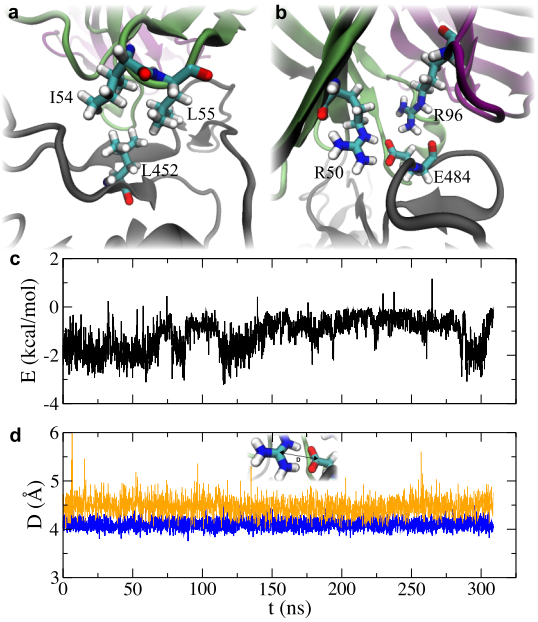

Figure 2. Favorable interactions between LY-CoV555 and the RBD. (a,b) Illustrations of favorable coordinations for L452 and E484 that are mutated into R452 and Q484 in the Kappa variant. (c) Time-dependent interaction energies between L452 in the RBD and I54/L55 in the V^H domain of (LY-CoV555). (d) Time-dependent distances between the CZ atom in (R50 or R96) and the CD atom in E484. The inset illustrates the definition of the distance *D*. Results for the salt bridges R50-E484 and R96-E484 are colored in blue and orange, respectively.

reduces the potential energy by 1.2 kcal/mol averagely. In addition, two energy levels can be discerned in the time-dependent interactions (Figure 2c), resulting from the fact that I54 can temporarily move away from L452 from time to time due to thermal fluctuations. When both I54 and L55 interacted with L452, the mean interaction energy is about −2 kcal/mol. However, with only L55 bound with L452, the interaction was weaker and the mean energy is only about −0.5 kcal/mol (Figure 2c).

To demonstrate that two salt bridges shown in Figure 2b were stable, we calculated time-dependent characteristic distance *D*, defined as the distance between the CZ atom in R50 (or R96) and the CD atom in E484 (see the inset in Figure 2d). Figure 2d shows that the time-dependent distance *D* between R50 and E484 is nearly constant and the average distance is 4.1 Å. The salt bridge between R96 and E484 has a different pose (Figure 2b), leading to a larger average distance of 4.5 Å. Noticeably, the fluctuation in time-dependent distances is larger for the salt bridge between R96 and E484 than for the salt bridge between R50 and E484, suggesting that the former salt bridge is relatively weaker. Overall, the local structure formed by E484, R50, and R96 was stable (Movie S1 in Supporting Information) because these two salt bridges were actually buried inside the protein complex (Figure S1 in Supporting Information). Note that generally a water-exposed salt bridge can form and break frequently and thus their distances can have two different mean values corresponding to formed and broken states of the salt bridge.[9]

FEP Calculations for L452R and E484Q Mutations in the Kappa Variant. Unfortunately, the importance of L452 and E484 in stabilizing the LY-CoV555's binding with the RBD as shown above also indicates that the L452R and E484Q mutations can result in strong resistance to LY-CoV555. Here, we performed free energy perturbation (FEP) calculations[21] to obtain the binding free energy change ($\Delta\Delta G$) induced by the L452R and E484Q mutations. As required in FEP calculations, we performed 170 ns long MD simulations of the RBD in a 0.15 M KCl electrolyte (a free state), as shown in Figure S2a in Supporting Information. Generally, $\Delta\Delta G = \Delta G_a - \Delta G_b$ for each mutation on the RBD, where ΔG_a and ΔG_b are free energy changes for the bound state (Figure 1a) and the free state, respectively. Original data for ΔG_a and ΔG_b are provided in Tables S1 and S2 in the Supporting Information. Interestingly, the saturated RMSD values for RBD's backbone atoms are around 2 Å (Figure S2b in Supporting Information) that is larger than the one (1.5 Å) for the complex, which is due to the flexible coil (containing E484) in the free state (Movie S2 in Supporting Information). While in the bound state, the same coil is docked at the LY-CoV555's interface (see Figure 2b) and thus less flexible. It is worth noting that due to the flexibility of the abovementioned coil, in the Beta variant, the mutated K484 residue can move toward E75 in ACE2 and form a salt bridge,[9] enhancing the binding affinity. With protein structures for both bound and free states in respective MD simulations, we applied the FEP alchemy method to obtain the binding free energy difference for L452R and E484Q mutations on the RBD. The protocol is described in the Methods section, and the detailed one can be found in previous works.[9]

During a typical FEP calculation, the original and new residues gradually disappear and appear, respectively. After the L452R mutation, Figure 3a shows R452 being in contact with

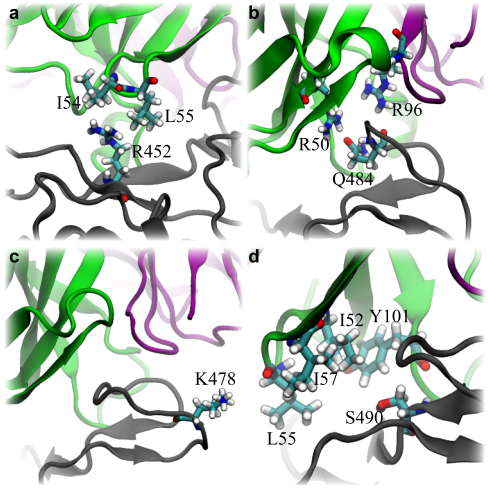

Figure 3. Interactions between LY-CoV555 and the variants' RBD. (a) Illustrations of unfavorable interfacial coordinations for L452R. (b) Illustrations of unfavorable interfacial coordinations for E484Q. (c) Illustrations of interfacial coordinations for T478K. (d) Illustrations of unfavorable interfacial coordinations for F490S. The RBD, V^L, and V^H are colored in gray, green, and purple, respectively. Key residues at the interface are in the stick representation.

the hydrophobic I54 and L55 residues (low dielectric media) in LY-CoV555. However, in the free state, R452 is surrounded by water/ions (high dielectric media), suggesting that it is unfavorable for R452 to be at the interface between RBD-v and LY-CoV555. The rigorous FEP calculation yielded $\Delta\Delta G$ of 3.04 kcal/mol, corroborating that the L452R mutation is energetically unfavorable. Our FEP result together with the

https://doi.org/10.1021/acs.jcim.1c01058
J. Chem. Inf. Model. 2021, 61, 5133−5140

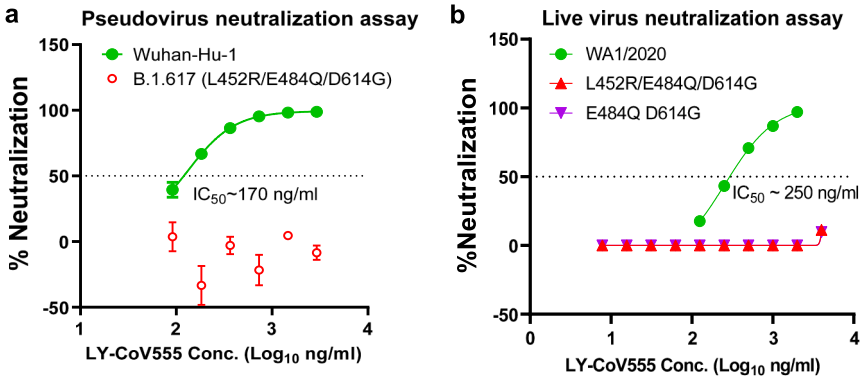

Figure 4. L452R/E484Q confers escape from LY-CoV555 in the experiment. (a) LY-CoV555 of different concentrations was added to pseudovirions bearing the wild type Wuhan-Huh-1 spike or sequences containing triple mutations found in the Kappa variant (L452R/E484Q/D614G). Neutralization was measured in the 293T-hACE2 cell line. (b) Plaque reduction neutralization assays were performed to evaluate the neutralizing ability of LY-CoV555 against WA1/2020, recombinant virus containing L452R/E484Q/D614G or E484Q/D614G.

role of L452 in the interfacial hydrophobic interaction (Figure 2a) provides theoretical explanations on why mutations of L452 to charged E, D, R, and K residues are highly evasive for LY-CoV555 observed in experiments.[22]

Figure 3b shows that after the E484Q mutation, Q484 was away from R96 and formed a hydrogen bond with R50. Compared with the local coordinations before the E484Q mutation (Figure 2b), the local interfacial interaction was significantly weakened after the removal of two salt bridges that were buried inside the complex and stabilized the entire complex (see Figure S2 in Supporting Information). Overall, the E484Q mutation yields an extra charge ($+e$, where e is the elementary charge) buried inside the low dielectric protein media, which is highly unfavorable from the free energy point of view. From the FEP calculation, $\Delta\Delta G \sim 22.22$ kcal/mol, indicating a much reduced binding affinity between RBD-v and LY-CoV555. Note that the result of $\Delta\Delta G$ is seemingly large but is consistent with the previous result that the removal of one buried salt bridge yields $\Delta\Delta G$ of about 10 kcal/mol.[9] Additionally, $\Delta\Delta G$ can be smaller if a K^+ ion arrives at the mutation site, which is not considered in the current calculation. Taking all these together, it is concluded that LY-CoV555 cannot bind RBD-v (of the Kappa variant).

E484Q and L452R/E484Q Confer Escape from LY-CoV555 in Experiment. To experimentally test the possible antibody escape conferred by mutations within the Kappa variant spike protein, we performed neutralization assays using lentiviral pseudovirions that bear the spike protein of the Wuhan-Hu-1 isolate or that of the Kappa variant (L452R/E484Q/D614G). As shown in Figure 4a, the half maximal inhibitory concentration (IC_{50}) of LY-CoV555 was around 170 ng/mL against pseudovirions bearing the Wuhan-Hu-1 spike protein but became unmeasurable against the Kappa variant, indicating that L452R/E484Q mutations completely rendered the variant nonsensitive to LY-CoV555.

To corroborate this finding, we then generated three recombinant live viruses using a 7-plasmid SARS-CoV-2 reverse genetics system.[23] All three recombinant viruses, including the wild type SARS-CoV-2-WA1/2020 (the first isolate reported in the U.S.) and mutants with L452R/E484Q/D614G or E484Q/D614G within the WA1 backbone, propagated similarly in Vero E6 cells. We then performed plaque reduction neutralization assays to determine the IC_{50} of LY-CoV555 against each of the recombinant viruses. Comparable to what was observed in the pseudovirion-based neutralization assay, the IC_{50} of LY-CoV555 against WA1/2020 was around 250 ng/mL. By contrast, LY-CoV555 displayed no neutralization against recombinant viruses carrying E484Q or L452R/E484Q even at the highest concentration tested (4 μg/mL). These experimental results are consistent with our predictions from MD simulation. More importantly, the experiment confirms that E484Q is more important for the variant to escape LY-CoV555.

FEP Calculations for L452R and T478K Mutations in the Delta Variant. Similar to the Kappa variant, the Delta variant also contains the L452R mutations. For the same reason stated above, the L452R mutation can cause the Delta variant to evade LY-CoV555 as well. In addition, the Delta variant carries the T478K mutation in the RBD. Using the same FEP method, we evaluate effects of the T478K mutation on the binding between the RBD and LY-CoV555. The result for $\Delta\Delta G$ from FEP calculations is listed in Table 1. Compared with the free energy change for the T478K mutation in the free state (i.e., the RBD alone), in the bound state (i.e., the complex of RBD and LY-CoV555), the free energy change for the same mutation is larger only by 0.70 kcal/mol, which suggests that the T478K mutation moderately weakens the binding between the RBD and LY-CoV555.

Table 1. $\Delta\Delta G$ for Various Mutations from FEP Calculations

mutations	$\Delta\Delta G$ (kcal/mol)
L452R	3.04 ± 0.63
E484Q	22.22 ± 0.42
T478K	0.70 ± 0.36
L452Q	0.95 ± 0.24
F490S	2.68 ± 0.15

Figure 3c shows that K478 in the RBD-v is not inside the binding interface between RBD-v and LY-CoV555, and therefore, the T478K mutation does not directly affect the RBD's binding affinity with LY-CoV555. However, compared to the bulk water environment (with a high dielectric constant), LY-CoV555 close to the charged K478 residue provides a low-dielectric media. The latter causes a less electric screening and a slight increase of the free energy (0.70 kcal/mol) for the entire system. Adding together, the double mutation yields a net $\Delta\Delta G \sim 3.74$ kcal/mol, given that L452 and T478 are not close to each other in the RBD (or their

https://doi.org/10.1021/acs.jcim.1c01058
J. Chem. Inf. Model. 2021, 61, 5133−5140

interference is negligible). Therefore, it is concluded that the Delta variant can also evade LY-CoV555.

It is well known that the Delta variant is much more transmissive than the wild-type SARS-CoV-2 and all other variants. To date, it is still not clear whether the T478K mutation could lead to an increased binding affinity between RBD-v and hACE2. Meanwhile, in the experiment, it was found that the P681R mutation in the spike protein (not in the RBD-v) plays a key role in the Alpha-to-Delta variant replacement, by allowing for a more efficient cleavage by furin and thus enhancing the viral reproduction.[24] However, the Kappa variant also contains the P681R mutation and it is intriguing to know why the Delta variant can dominate the Kappa variant. Especially from our abovementioned calculations, it appears that the net $\Delta\Delta G$ for the double mutations in the Kappa variant is much larger than that in the Delta variant, suggesting that the Kappa variant can dodge LY-CoV555 more effectively. Further studies on the Delta's high transmissibility are highly demanded.

FEP Calculations for L452Q and F490S Mutations in the Lambda Variant. Recently, the emergent Lambda variant has spread to many countries and become a VOI. Remarkably, the Lambda variant also contains a mutation to L452. Instead of the L452R mutation in the Kappa and Delta variants, the similar mutation is L452Q. Thus, the molecular mechanism of destabilizing the RBD-v's binding with LY-CoV555 can be derived correspondingly. As shown in Figure 2a, L452 in the RBD coordinates I54 and L55 in LY-CoV555 through the hydrophobic interaction. After the L452Q mutation, Q452 is hydrophilic and orients itself toward water, which weakens the local interfacial binding affinity. From our FEP calculations (Table 1), the $\Delta\Delta G$ value is about 1 kcal/mol (unfavorable for the complex binding).

Additionally, the Lambda variant has an uncommon mutation F490S in the RBD, which we show below is highly beneficial for the Lambda variant. The result from FEP calculations (Table 1) shows that the $\Delta\Delta G$ for the F490S mutation is 2.68 kcal/mol, indicating that this mutation is also very evasive to LY-CoV555. Before the F490S mutation, F490 coordinates four nearby hydrophobic residues, namely, Y101, I52, I57, and L55, in LY-CoV555 (the V^H domain) and this favorable interfacial interaction is abolished after the mutation. As shown in Figure 3d, the hydrophilic S490 (smaller than the hydrophobic F490) is not in contact with those four residues and preferentially interacts with surrounding water instead.

All together, the net $\Delta\Delta G$ for the double mutations in Lambda is 3.63 kcal/mol. However, we note that both L452 and F490 are in contact with L55 in LY-CoV555 (Figure 3a,d). Thus, the simultaneous mutations of L452R and F490S might be synergistic by further destabilizing the interfacial contact. Overall, for the potential of evading LY-CoV555, the Delta and Lambda variants are comparable, while the Kappa variant is the most evasive one.

DISCUSSION AND CONCLUSIONS

In the *in silico* part of this study, we assumed that LY-CoV555 targets RBD-v at the same epitope, which leads to our conclusion that based on FEP calculations the double mutations L452R and E484Q in the Kappa variant can significantly reduce LY-CoV555's binding affinity to RBD-v. Through MD simulation, we highlighted the molecular mechanism on how LY-CoV555 can be efficaciously bound with wild-type RBD but fails to bind RBD-v in Kappa, Delta, or Lambda variant. Our alchemy FEP calculations show that binding free energy changes for L452R and E484K mutations are 3.04 and 22.22 kcal/mol, respectively, indicating that these two mutations substantially weaken the binding between RBD-v and LY-CoV555 and thus are evasive. However, we point out that these two mutations are not resistant to LY-CoV016 (or Etesevimab), as shown in Figure S3 in the Supporting Information. It is worth noting that the recent sub-lineage of B.1.617 (dubbed as Delta+) contains the K417N mutation, allowing the virus to escape LY-CoV016[11,18] as well. In addition, we carried out FEP calculations for newly emergent variants Delta and Lambda and concluded that these two variants are also evasive to LY-CoV555 (but not to LY-CoV016).

We also performed an experiment to verify the simulation results. Applying both pseudovirions and live virus-based neutralization assays, we demonstrated that LY-CoV555 can neutralize original SARS-CoV-2 virus but completely lost neutralizing activity against the Kappa variant carrying L452R and E484Q mutations. Additionally, we show that the E484Q mutation alone can cause LY-CoV555 to lose neutralizing activity as well, which is consistent with the much larger free energy change ($\Delta\Delta G$) found in MD simulation (Table 1). Overall, both experimental and simulation results unanimously suggest that LY-CoV555 cannot target these new variants and thus should not be used in clinics. Note that we published these results in a bioRxiv paper of ours[25] in May and later (nearly at the same time) Laurini et al. published similar results in bioRxiv[26] (corroborating that these variants can evade LY-CoV555), using the MM-PBSA-based approach for calculating free energy changes (in contrast to the FEP method in our work).

Besides LY-CoV555, these mutations in the Kappa, Delta, and Lambda variants might reduce the binding affinity with other antibodies as well. For example, E484 coordinates N52/S55 (through hydrogen bonds) in the complex of the RBD and the antibody S2M11, and consequently, the mutation E484Q might weaken the complex,[19] which warrants further studies.

With the revealed molecular mechanism for RBD's binding with LY-CoV555 and energetics for mutations, it becomes possible to design or engineer a more efficacious antibody drug targeting these emergent variants. Meanwhile, it is advantageous to stay one-step ahead of SARA-CoV-2 by considering what other evasive mutations it could evolve. Overall, our work shed light on the mechanism of evasive mutations of the newly emergent variants and can facilitate the design of new antibody drugs specifically targeting these variants.

METHODS

MD Simulations. We carried out all-atom MD simulations for the complex of the RBD and the Fab of LY-CoV555 (PDB code: 7KMG) using the NAMD2.13 package[27] running on the IBM Power Cluster. The complex was solvated in a cubic water box that measures about $110 \times 110 \times 110$ Å^3. K^+ and Cl^- were added to neutralize the entire simulation system and set the ion concentration to be 0.15 M (Figure 1a). The final simulation system comprises 132,308 atoms. The built system was first minimized for 10 ps and further equilibrated for 1000 ps in the *NPT* ensemble (P ~ 1 bar and T ~ 300 K), with atoms in the backbones harmonically restrained (spring constant k = 1 kcal/mol/Å^2). The production run was performed in the *NPT* ensemble without any restraint. The same approach was applied in the production run for the RBD

https://doi.org/10.1021/acs.jcim.1c01058
J. Chem. Inf. Model. 2021, 61, 5133−5140

in a 0.15 M KCl electrolyte (Figure S1 in Supporting Information), a free state required in the FEP calculations (see below). The water box for the RBD-only simulation also measures about 110 × 110 × 110 Å^3. Note that the same system size for the bound and free states is required for FEP calculations for mutations with a net charge change.

We used the CHARMM36m force field[28] for proteins, the TIP3P model[29,30] for water, and the standard force field[31] for K^+ and Cl^-. The periodic boundary conditions were applied in all three dimensions. Long-range Coulomb interactions were calculated using particle-mesh Ewald (PME) full electrostatics with the grid size of about 1 Å in each dimension. The pairwise vdW energies were computed using a smooth (10−12 Å) cutoff. The temperature T was kept at 300 K by applying the Langevin thermostat,[32] while the pressure was maintained at 1 bar using the Nosé−Hoover method.[33] With the SETTLE algorithm[34] enabled to keep all bonds rigid, the simulation time-step was 2 fs for bonded and nonbonded (including vdW, angle, improper, and dihedral) interactions, and the time-step for Coulomb interactions was 4 fs, with the multiple time-step algorithm.[35]

FEP Calculations. After equilibrating the structures in bound and free states, we performed FEP calculations.[21] In the perturbation method, many intermediate stages (denoted by λ) whose Hamiltonian $H(\lambda) = \lambda H_f + (1 - \lambda)H_i$ are inserted between the initial and final states to yield a high accuracy. With the softcore potential enabled, λ in each FEP calculation for the bound or free state varies from 0 to 1.0 in 20 perturbation windows (lasting 300 ps in each window), yielding gradual (and progressive) annihilation and exnihilation processes for L452 and R452 (or for E484 and Q484), respectively. More detailed procedures can be found in our previous work.[11,18] In FEP runs for the E484Q mutation, the net charge of the MD system changed from −1 to 0e (where e is the elementary charge). It is important to have similar sizes of the simulation systems for the free and the bound states,[36,37] so that the energy shifts from the Ewald summation (due to the net charge in the final simulation system) approximately cancel out when calculating $\Delta\Delta G$. The same approaches were applied to investigate mutations in the Delta and Kappa variants.

SARS-CoV-2 Pseudovirus Production and Neutralization. SARS-CoV-2 pseudovirus production and neutralization assay human codon-optimized cDNA encoding SARS-CoV-2 S glycoprotein of the Wuhan-Hu-1 isolate (NC_045512) or the Kappa variant was synthesized by GenScript and cloned into eukaryotic cell expression vector pcDNA 3.1 between the BamHI and XhoI sites.[38] Pseudovirions were produced by co-transfection of Lenti-X 293T cells with psPAX2, pTRIP-luc, and SARS-CoV-2 S expressing plasmid using Lipofectamine 3000. The supernatants were harvested at 48 and 72 h post-transfection and filtered through 0.45 μm membranes. For the antibody neutralization assay, 50 μL of SARS-CoV-2 S pseudovirions was preincubated with an equal volume of medium containing LY-CoV555 at varying dilutions at room temperature for 1 h, and then, virus−antibody mixtures were added to 293T-hACE2 cells in a 96-well plate. After a 3 h incubation, the inoculum was replaced with fresh medium. Cells were lysed 48 h later, and luciferase activity was measured using the luciferin-containing substrate. Controls included cell-only control and virus without any antibody control. The end-point titers were calculated as the last serum dilution resulting in at least 50% SARS-CoV-2 neutralization. The amount of pseudovirions used in this assay has been determined to give rise to a target input 5 × 10^5 to 10^7 RLU/mL, under which condition the neutralization law is observed.

Production of SARS-CoV-2 Recombinant. SARS-CoV-2 recombinant viruses containing 2019-nCoV/USA_WA1/2020 sequence or mutations (L452R/E484Q/D614G, E484Q/D614G) in the spike protein of the Kappa variant were generated using a 7-plasmid reverse genetic system, which was based on the virus strain (2019-nCoV/USA_WA1/2020) isolated from the first reported SARS-CoV-2 case in the US.[23] The initial 7 plasmids were generous gifts from Dr. P.-Y. Shi (UTMB). Upon receipt, fragment 4 was subsequently subcloned into a low-copy plasmid pSMART LCAmp (Lucigen) to increase stability. The standard molecular biology technique was employed to create mutations. In vitro transcription and electroporation were carried following procedures that were detailed elsewhere.[39] Recombinant viruses were further deep sequenced at the FDA core facility to confirm the presence of mutations.

Plaque Reduction Neutralization Assay (PRNT). 40 PFU recombinant virus was incubated with 2-fold serial antibody dilutions in a round bottom plate at 37 °C for 1 h. The virus−antibody mixture was then added to a 24-well plate with confluent Vero E6 cells. After 1 h, the mixture was removed and replenished with fresh MEM containing 2% FBS. Cells were incubated at 37 °C for an additional 48 h and then fixed with 4% paraformaldehyde, followed by staining of cells with 0.1% crystal violet in 20% methanol. The $PRNT_{50}$ titers were calculated as the last serum dilution resulting in at least 50% SARS-CoV-2 neutralization.

DATA AND SOFTWARE AVAILABILITY

We provided data files for the equilibrated structure of the LY-CoV555/RBD complex: equilibrated-complex.pdb. We used the softwares NAMD and VMD in this work that can be downloaded freely from the website https://www.ks.uiuc.edu.

ASSOCIATED CONTENT

Supporting Information

The Supporting Information is available free of charge at https://pubs.acs.org/doi/10.1021/acs.jcim.1c01058.

Movie showing the stable interfacial salt bridge binding (E484-R50-R96.mpg) (MPG)

Movie showing the flexible coil (containing E484) in the RBD-only simulation (MPG)

Equilibrated structure of the LY-COV555/RBD complex (PDB)

Illustration of buried salt bridges inside the complex; MD simulation of the RBD-only system; illustration of the complex of LY-CoV016 and the RBD (PDF)

AUTHOR INFORMATION

Corresponding Authors

Tony T. Wang − *Division of Viral Products, Center for Biologics Evaluation and Research, Food and Drug Administration, Silver Spring, Maryland 20993, United States*; Email: Tony.Wang@fda.hhs.gov

Binquan Luan − *Computational Biological Center, IBM Thomas J. Watson Research, Yorktown Heights, New York 10598, United States*; orcid.org/0000-0002-9414-5379; Email: bluan@us.ibm.com

Authors

Shufeng Liu − *Division of Viral Products, Center for Biologics Evaluation and Research, Food and Drug Administration, Silver Spring, Maryland 20993, United States*

Tien Huynh − *Computational Biological Center, IBM Thomas J. Watson Research, Yorktown Heights, New York 10598, United States*

Charles B. Stauft − *Division of Viral Products, Center for Biologics Evaluation and Research, Food and Drug Administration, Silver Spring, Maryland 20993, United States*

Complete contact information is available at: https://pubs.acs.org/10.1021/acs.jcim.1c01058

Notes

The authors declare no competing financial interest.

■ ACKNOWLEDGMENTS

T.H. and B.L. gratefully acknowledge the computing resource from the IBM Cognitive Computing Program. S.L., C.B.S., and T.T.W. are grateful to Dr. P.-Y. Shi (UTMB), who generously shared the 7-plasmid SARS-CoV-2 reverse genetics system. This study was partly supported by a FDA MCM CHALLENGE 21 Grant.

■ REFERENCES

(1) Sanjuán, R.; Domingo-Calap, P. Mechanisms of viral mutation. *Cell. Mol. Life Sci.* **2016**, *73*, 4433−4448.

(2) Shang, J.; Ye, G.; Shi, K.; Wan, Y.; Luo, C.; Aihara, H.; Geng, Q.; Auerbach, A.; Li, F. Structural basis of receptor recognition by SARS-CoV-2. *Nature* **2020**, *581*, 221−224.

(3) Du, L.; He, Y.; Zhou, Y.; Liu, S.; Zheng, B.-J.; Jiang, S. The spike protein of SARS-CoV—a target for vaccine and therapeutic development. *Nat. Rev. Microbiol.* **2009**, *7*, 226−236.

(4) Li, Q.; Wu, J.; Nie, J.; Zhang, L.; Hao, H.; Liu, S.; Zhao, C.; Zhang, Q.; Liu, H.; Nie, L.; Qin, H.; Wang, M.; Lu, Q.; Li, X.; Sun, Q.; Liu, J.; Zhang, L.; Li, X.; Huang, W.; Wang, Y. The impact of mutations in SARS-CoV-2 spike on viral infectivity and antigenicity. *Cell* **2020**, *182*, 1284−1294.

(5) Korber, B.; Fischer, W. M.; Gnanakaran, S.; Yoon, H.; Theiler, J.; Abfalterer, W.; Hengartner, N.; Giorgi, E. E.; Bhattacharya, T.; Foley, B.; Hastie, K. M.; Parker, M. D.; Partridge, D. G.; Evans, C. M.; Freeman, T. M.; de Silva, T. I.; McDanal, C.; Perez, L. G.; Tang, H.; Moon-Walker, A.; Whelan, S. P.; LaBranche, C. C.; Saphire, E. O.; Montefiori, D. C.; Angyal, A.; Brown, R. L.; Carrilero, L.; Green, L. R.; Groves, D. C.; Johnson, K. J.; Keeley, A. J.; Lindsey, B. B.; Parsons, P. J.; Raza, M.; Rowland-Jones, S.; Smith, N.; Tucker, R. M.; Wang, D.; Wyles, M. D.; Sheffield COVID-19 Genomics Group. Tracking changes in SARS-CoV-2 Spike: evidence that D614G increases infectivity of the COVID-19 virus. *Cell* **2020**, *182*, 812−827.

(6) Plante, J. A.; Liu, Y.; Liu, J.; Xia, H.; Johnson, B. A.; Lokugamage, K. G.; Zhang, X.; Muruato, A. E.; Zou, J.; Fontes-Garfias, C. R.; Mirchandani, D.; Scharton, D.; Bilello, J. P.; Ku, Z.; An, Z.; Kalveram, B.; Freiberg, A. N.; Menachery, V. D.; Xie, X.; Plante, K. S.; Weaver, S. C.; Shi, P.-Y. Spike mutation D614G alters SARS-CoV-2 fitness. *Nature* **2021**, *592*, 116−121.

(7) Chan, K. K.; Tan, T. J. C.; Narayanan, K. K.; Procko, E. An engineered decoy receptor for SARS-CoV-2 broadly binds protein S sequence variants. *Sci. Adv.* **2021**, *7*, No. eabf1738.

(8) Starr, T. N.; Greaney, A. J.; Hilton, S. K.; Ellis, D.; Crawford, K. H. D.; Dingens, A. S.; Navarro, M. J.; Bowen, J. E.; Tortorici, M. A.; Walls, A. C.; King, N. P.; Veesler, D.; Bloom, J. D. Deep mutational scanning of SARS-CoV-2 receptor binding domain reveals constraints on folding and ACE2 binding. *Cell* **2020**, *182*, 1295−1310.

(9) Luan, B.; Wang, H.; Huynh, T. Enhanced binding of the N501Y-mutated SARS-CoV-2 spike protein to the human ACE2 receptor: insights from molecular dynamics simulations. *FEBS Lett.* **2021**, *595*, 1454−1461.

(10) Wang, P.; Nair, M. S.; Liu, L.; Iketani, S.; Luo, Y.; Guo, Y.; Wang, M.; Yu, J.; Zhang, B.; Kwong, P. D.; Graham, B. S.; Mascola, J. R.; Chang, J. Y.; Yin, M. T.; Sobieszczyk, M.; Kyratsous, C. A.; Shapiro, L.; Sheng, Z.; Huang, Y.; Ho, D. D. Antibody resistance of SARS-CoV-2 variants B. 1.351 and B. 1.1. 7. *Nature* **2021**, *593*, 130−135.

(11) Luan, B.; Huynh, T. Insights into SARS-CoV-2's Mutations for Evading Human Antibodies: Sacrifice and Survival. *J. Med. Chem.* **2021**, DOI: 10.1021/acs.jmedchem.1c00311.

(12) Deng, X.; Garcia-Knight, M. A.; Khalid, M. M.; Servellita, V.; Wang, C.; Morris, M. K.; Sotomayor-González, A.; Glasner, D. R.; Reyes, K. R.; Gliwa, A. S.; Reddy, N. P.; Sanchez San Martin, C.; Federman, S.; Cheng, J.; Balcerek, J.; Taylor, J.; Streithorst, J. A.; Miller, S.; Sreekumar, B.; Chen, P. Y.; Schulze-Gahmen, U.; Taha, T. Y.; Hayashi, J. M.; Simoneau, C. R.; Kumar, G. R.; McMahon, S.; Lidsky, P. V.; Xiao, Y.; Hemarajata, P.; Green, N. M.; Espinosa, A.; Kath, C.; Haw, M.; Bell, J.; Hacker, J. K.; Hanson, C.; Wadford, D. A.; Anaya, C.; Ferguson, D.; Frankino, P. A.; Shivram, H.; Lareau, L. F.; Wyman, S. K.; Ott, M.; Andino, R.; Chiu, C. Y. Transmission, infectivity, and neutralization of a spike L452R SARS-CoV-2 variant. *Cell* **2021**, *184*, 3426.

(13) Karplus, M.; McCammon, J. Molecular dynamics simulations of biomolecules. *Nat. Struct. Biol.* **2002**, *9*, 646−652.

(14) Freddolino, P. L.; Harrison, C. B.; Liu, Y.; Schulten, K. Challenges in protein-folding simulations. *Nat. Phys.* **2010**, *6*, 751−758.

(15) Huynh, T.; Wang, H.; Luan, B. in silico Exploration of Molecular Mechanism of Clinically Oriented Drugs for Inhibiting SARS-CoV-2's Main Protease. *J. Phys. Chem. Lett.* **2020**, *11*, 4413−4420.

(16) Wang, Y.; Liu, M.; Gao, J. Enhanced receptor binding of SARS-CoV-2 through networks of hydrogen-bonding and hydrophobic interactions. *Proc. Natl. Acad. Sci. U.S.A.* **2020**, *117*, 13967.

(17) Jones, B. E.; Brown-Augsburger, P. L.; Corbett, K. S.; Westendorf, K.; Davies, J.; Cujec, T. P.; Wiethoff, C. M.; Blackbourne, J. L.; Heinz, B. A.; Foster, D.; Higgs, R. E.; Balasubramaniam, D.; Wang, L.; Bidshahri, R.; Kraft, L.; Hwang, Y.; Žentelis, S.; Jepson, K. R.; Goya, R.; Smith, M. A.; Collins, D. W.; Hinshaw, S. J.; Tycho, S. A.; Pellacani, D.; Xiang, P.; Muthuraman, K.; Sobhanifar, S.; Piper, M. H.; Triana, F. J.; Hendle, J.; Pustilnik, A.; Adams, A. C.; Berens, S. J.; Baric, R. S.; Martinez, D. R.; Cross, R. W.; Geisbert, T. W.; Borisevich, V.; Abiona, O.; Belli, H. M.; de Vries, M.; Mohamed, A.; Dittmann, M.; Samanovic, M.; Mulligan, M. J.; Goldsmith, J. A.; Hsieh, C. L.; Johnson, N. V.; Wrapp, D.; McLellan, J. S.; Barnhart, B. C.; Graham, B. S.; Mascola, J. R.; Hansen, C. L.; Falconer, E. The neutralizing antibody, LY-CoV555, protects against SARS-CoV-2 infection in non-human primates. *Sci. Transl. Med.* **2021**, *13*, No. eabf1906.

(18) Luan, B.; Huynh, T. In Silico Antibody Mutagenesis for Optimizing Its Binding to Spike Protein of Severe Acute Respiratory Syndrome Coronavirus 2. *J. Phys. Chem. Lett.* **2020**, *11*, 9781−9787.

(19) Tortorici, M. A.; Beltramello, M.; Lempp, F. A.; Pinto, D.; Dang, H. V.; Rosen, L. E.; McCallum, M.; Bowen, J.; Minola, A.; Jaconi, S.; Zatta, F.; De Marco, A.; Guarino, B.; Bianchi, S.; Lauron, E. J.; Tucker, H.; Zhou, J.; Peter, A.; Havenar-Daughton, C.; Wojcechowskyj, J. A.; Case, J. B.; Chen, R. E.; Kaiser, H.; Montiel-Ruiz, M.; Meury, M.; Czudnochowski, N.; Spreafico, R.; Dillen, J.; Ng, C.; Sprugasci, N.; Culap, K.; Benigni, F.; Abdelnabi, R.; Foo, S.-Y. C.; Schmid, M. A.; Cameroni, E.; Riva, A.; Gabrieli, A.; Galli, M.; Pizzuto, M. S.; Neyts, J.; Diamond, M. S.; Virgin, H. W.; Snell, G.; Corti, D.; Fink, K.; Veesler, D. Ultrapotent human antibodies protect against SARS-CoV-2 challenge via multiple mechanisms. *Science* **2020**, *370*, 950−957.

(20) Connolly, M. L. Solvent-Accessible Surfaces of Proteins and Nucleic Acids. *Science* **1983**, *221*, 709−713.

(21) Chipot, C.; Pohorille, A. *Free Energy Calculations*; Springer, 2007.

(22) Starr, T. N.; Greaney, A. J.; Dingens, A. S.; Bloom, J. D. Complete map of SARS-CoV-2 RBD mutations that escape the monoclonal antibody LY-CoV555 and its cocktail with LY-CoV016. *Cell Rep. Med.* **2021**, *2*, 100255.
(23) Xie, X.; Muruato, A.; Lokugamage, K. G.; Narayanan, K.; Zhang, X.; Zou, J.; Liu, J.; Schindewolf, C.; Bopp, N. E.; Aguilar, P. V.; Plante, K. S.; Weaver, S. C.; Makino, S.; LeDuc, J. W.; Menachery, V. D.; Shi, P.-Y. An infectious cDNA clone of SARS-CoV-2. *Cell Host Microbe* **2020**, *27*, 841−848.
(24) Liu, Y.; Liu, J.; Johnson, B. A.; Xia, H.; Ku, Z.; Schindewolf, C.; Widen, S. G.; An, Z.; Weaver, S.; Menachery, V. D.; Xie, X.; Shi, P. Y. Delta Spike P681R Mutation Enhances SARS-CoV-2 Fitness over Alpha Variant. **2021**, bioRxiv:2021.08.12.456173.
(25) Zhang, L.; Huynh, T.; Luan, B. In Silico Assessment of Antibody Drug Resistance to Bamlanivimab of SARS-CoV-2 Variant B. 1.617. **2021**, bioRxiv:2021.05.12.443826.
(26) Laurini, E.; Marson, D.; Aulic, S.; Fermeglia, A.; Pricl, S. In Silico Molecular-Based Rationale for SARS-CoV-2 Spike Circulating Mutations Able to Escape Bamlanivimab and Etesevimab Monoclonal Antibodies. **2021**, bioRxiv:2021.05.18.444605.
(27) Phillips, J. C.; Braun, R.; Wang, W.; Gumbart, J.; Tajkhorshid, E.; Villa, E.; Chipot, C.; Skeel, R. D.; Kalé, L.; Schulten, K. Scalable Molecular Dynamics with NAMD. *J. Comput. Chem.* **2005**, *26*, 1781−1802.
(28) Huang, J.; Rauscher, S.; Nawrocki, G.; Ran, T.; Feig, M.; De Groot, B. L.; Grubmüller, H.; MacKerell, A. D. CHARMM36m: an improved force field for folded and intrinsically disordered proteins. *Nat. Methods* **2017**, *14*, 71−73.
(29) Jorgensen, W. L.; Chandrasekhar, J.; Madura, J. D.; Impey, R. W.; Klein, M. L. Comparison of Simple Potential Functions for Simulating Liquid Water. *J. Chem. Phys.* **1983**, *79*, 926−935.
(30) Neria, E.; Fischer, S.; Karplus, M. Simulation of Activation Free Energies in Molecular Systems. *J. Chem. Phys.* **1996**, *105*, 1902−1921.
(31) Beglov, D.; Roux, B. Finite representation of an infinite bulk system: Solvent boundary potential for computer simulations. *J. Chem. Phys.* **1994**, *100*, 9050−9063.
(32) Allen, M. P.; Tildesley, D. J. *Computer Simulation of Liquids*; Oxford University Press: New York, 1987.
(33) Martyna, G. J.; Tobias, D. J.; Klein, M. L. Constant Pressure Molecular Dynamics Algorithms. *J. Chem. Phys.* **1994**, *101*, 4177−4189.
(34) Miyamoto, S.; Kollman, P. A. SETTLE: An Analytical Version of the SHAKE and RATTLE Algorithm for Rigid Water Molecules. *J. Comput. Chem.* **1992**, *13*, 952−962.
(35) Tuckerman, M.; Berne, B. J.; Martyna, G. J. Reversible multiple time scale molecular dynamics. *J. Chem. Phys.* **1992**, *97*, 1990−2001.
(36) Hummer, G.; Pratt, L. R.; García, A. E. Free Energy of Ionic Hydration. *J. Phys. Chem.* **1996**, *100*, 1206−1215.
(37) Luan, B.; Chen, K. L.; Zhou, R. Mechanism of Divalent-Ion-Induced Charge Inversion of Bacterial Membranes. *J. Phys. Chem. Lett.* **2016**, *7*, 2434−2438.
(38) Liu, S.; Selvaraj, P.; Lien, C. Z.; Nunez, I. A.; Wu, W. W.; Chou, C.-K.; Wang, T. T. The PRRA insert at the S1/S2 site modulates cellular tropism of SARS-CoV-2 and ACE2 usage by the closely related Bat RaTG13. *J. Virol.* **2021**, *95*, No. e01751.
(39) Xie, X.; Lokugamage, K. G.; Zhang, X.; Vu, M. N.; Muruato, A. E.; Menachery, V. D.; Shi, P.-Y. Engineering SARS-CoV-2 using a reverse genetic system. *Nat. Protoc.* **2021**, *16*, 1761−1784.

https://doi.org/10.1021/acs.jcim.1c01058
J. Chem. Inf. Model. 2021, 61, 5133−5140